Figure S1 (DiGregorio, Feller)

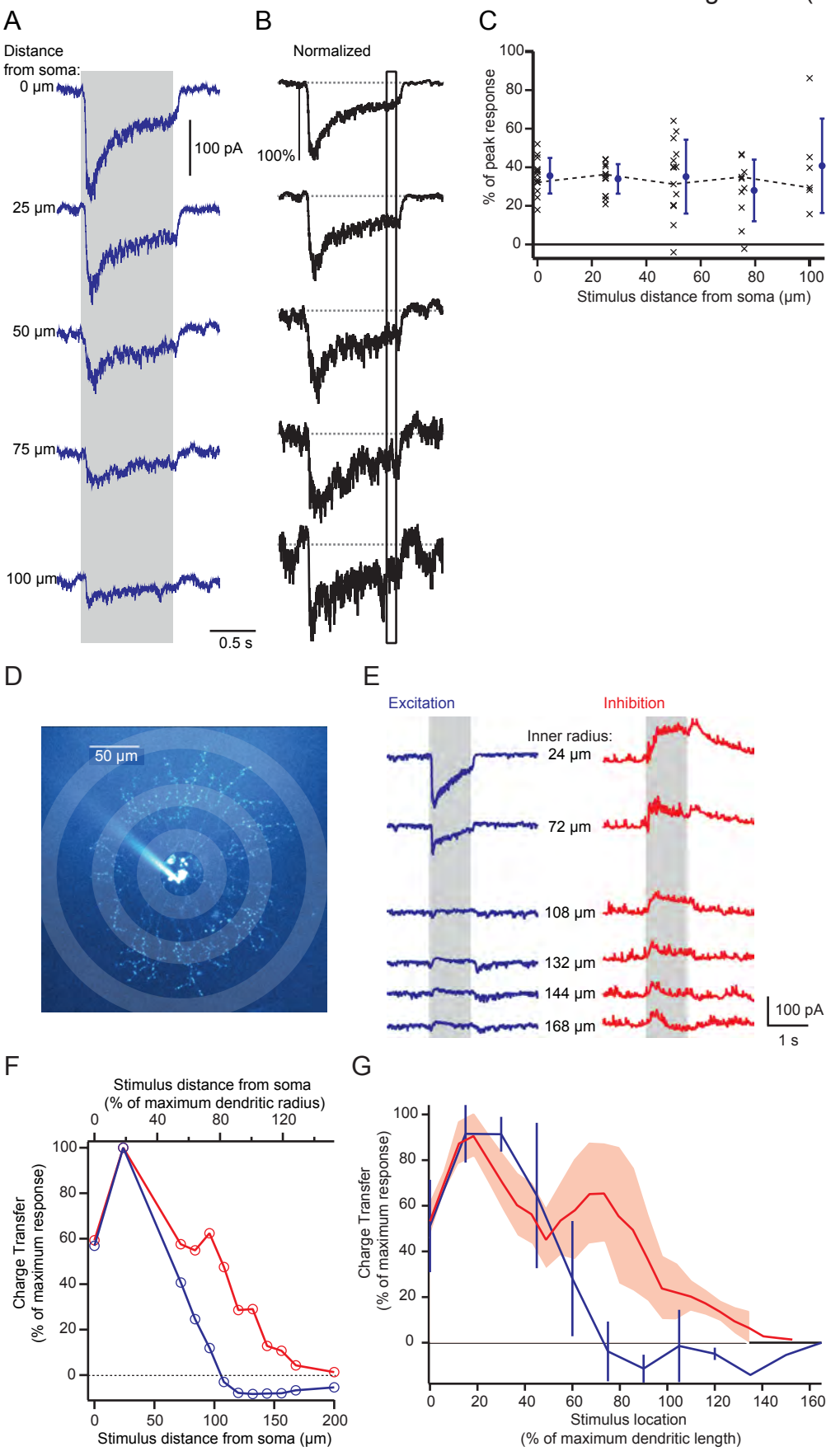

Figure S2 (DiGregorio, Feller)

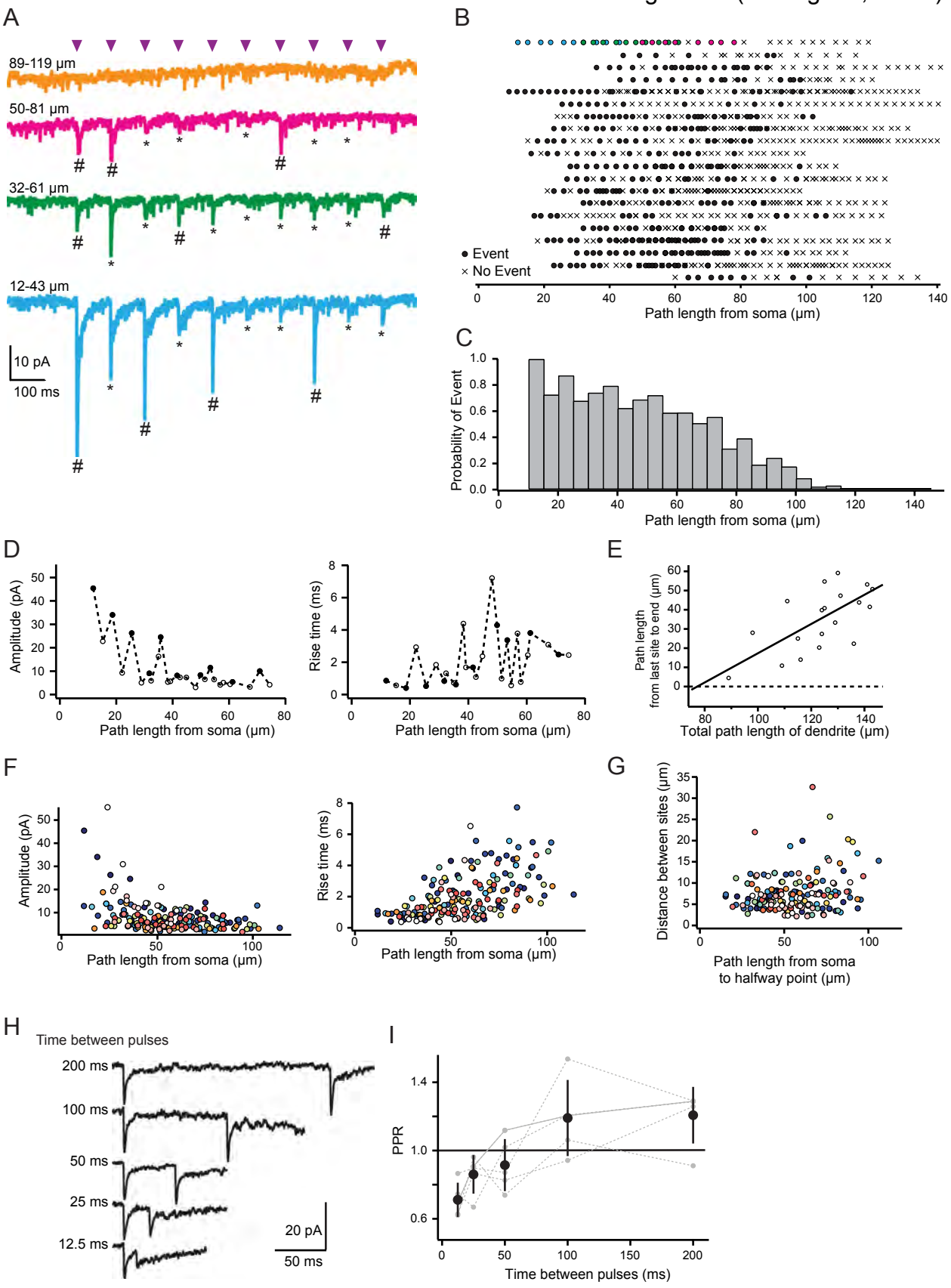

Figure S3 (DiGregorio, Feller)

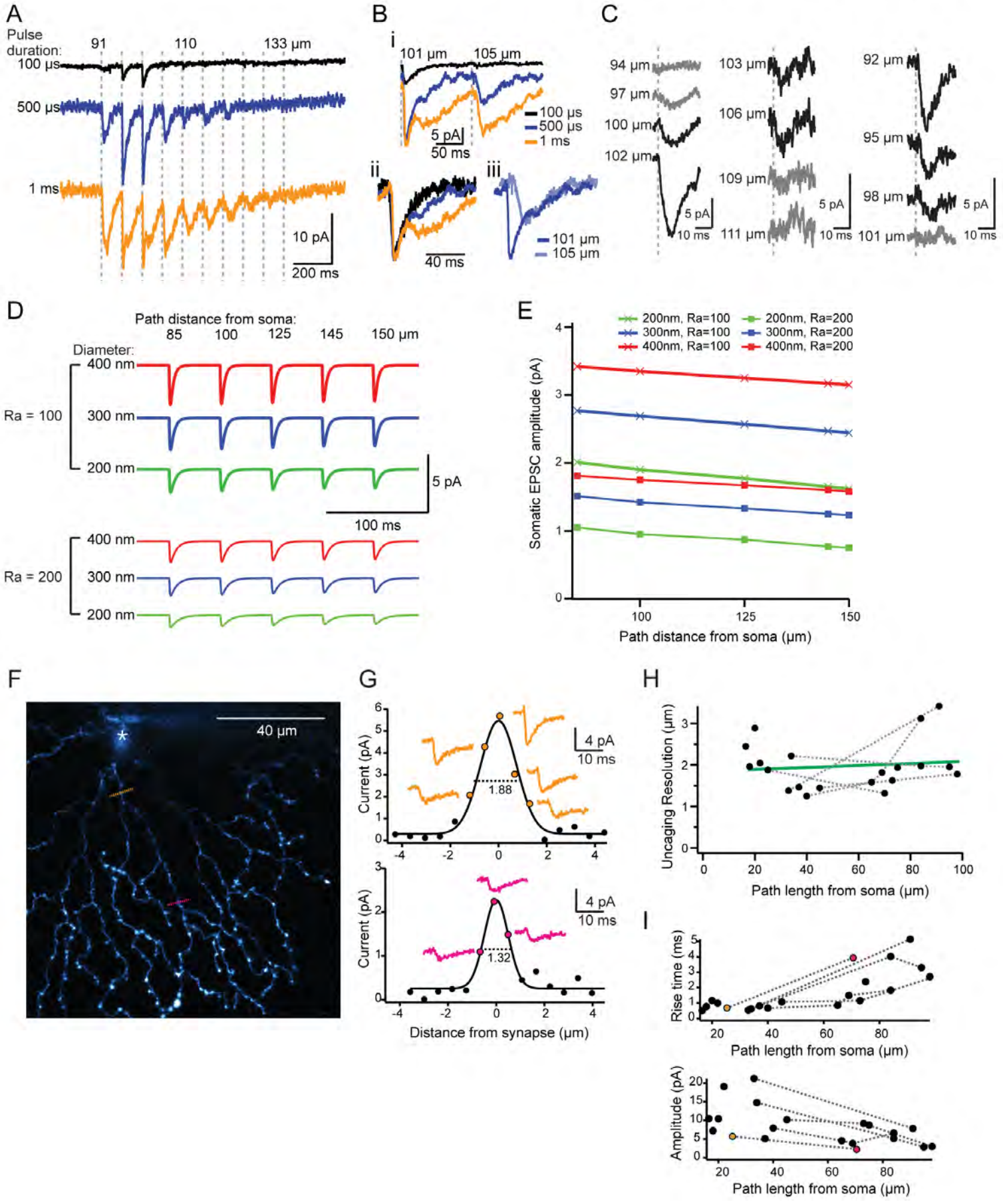

Figure S4 (DiGregorio, Feller)

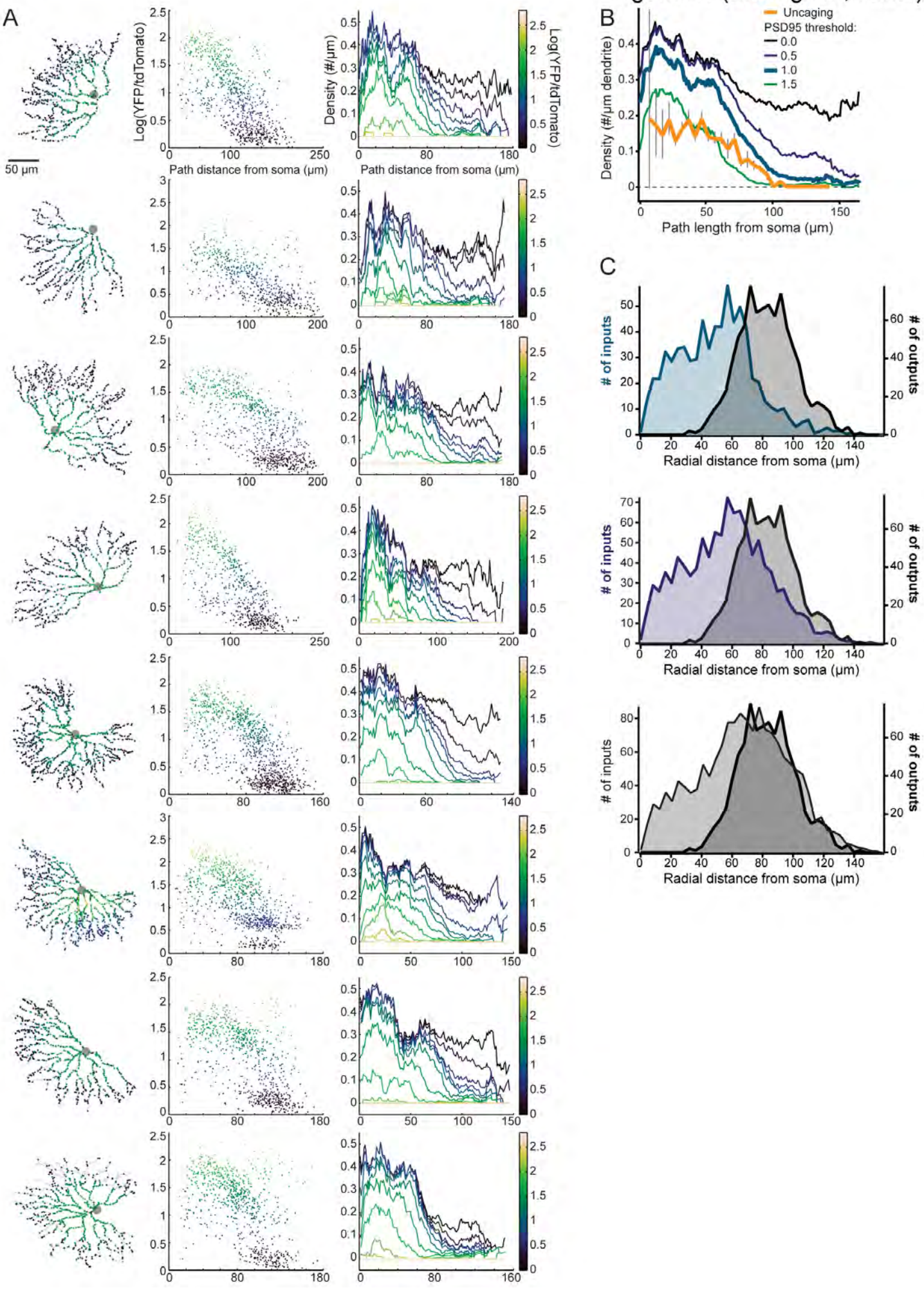

Figure S5 (DiGregorio, Feller)

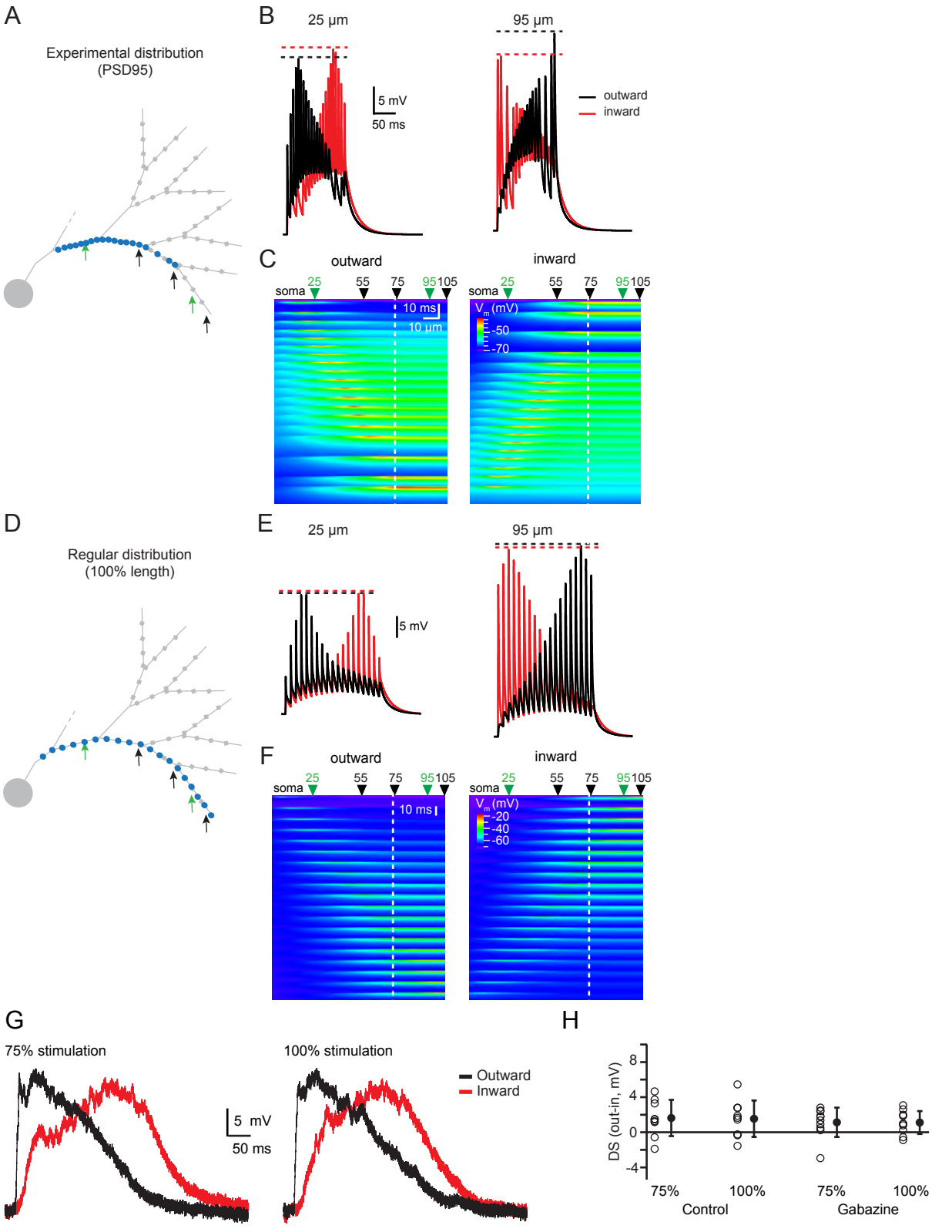

Figure S6 (DiGregorio, Feller)

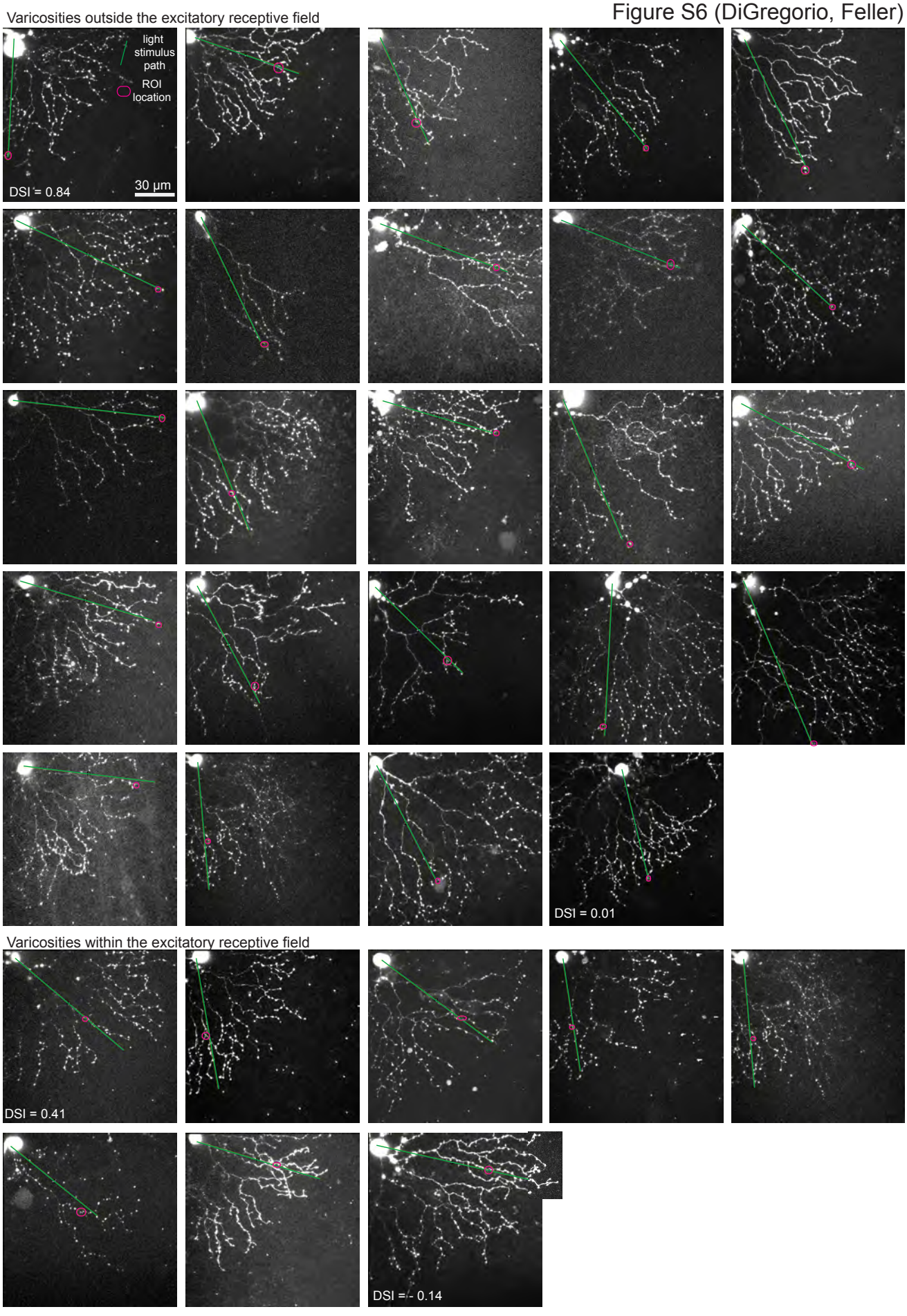

Figure S7 (DiGregorio, Feller)

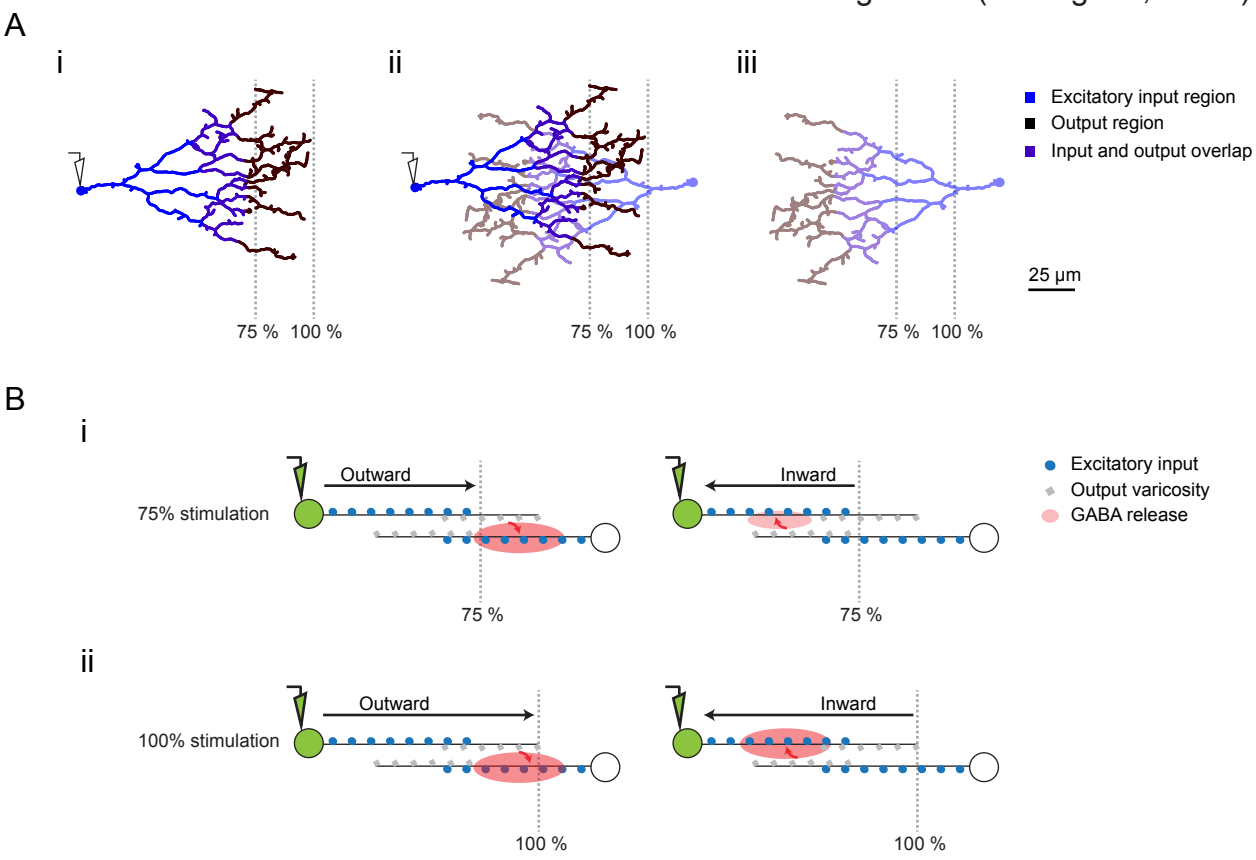

Supplemental Figure Legends

Figure S1. Kinetics of bipolar cell release onto SAC dendrites do not vary based on input location and inhibitory receptive field is larger than dendritic field. Related to Figure 1

A) Voltage clamp recordings (holding potential = -72 mV) in response to stimulation with 25 µm diameter spots centered at different distances from the soma. Grey box indicates the timing of the light stimulus. Traces are averages of 3 responses.

B) The same responses as in **A** normalized to the maximum amplitude (averaged over 50 ms window) during the first 300 ms of the response. The box indicates the period of time used to assess the sustained component of the response in **C**. Grey dotted lines mark the baseline.

C) Plot showing the amplitude of the sustained component of the response to spots at different distances from the soma as a percentage of the maximum amplitude. Black x are individual cells, blue dots are averages, error bar = S.D. Dotted line connects responses for the cell in **A** and **B**. N = 14 cells.

D) Schematic showing anatomical location of visual stimulation rings overlaid with 2-photon fluorescence projection of a SAC at low magnification (20x). Rings shown have an inner radius of 24, 72, and 132 µm. Ring thickness was 24 µm.

E). Voltage clamp recordings (holding potentials = -72 mV (blue) and 0 mV (red)) from the SAC in **D** during stimulation with stationary rings with different inner radii. Traces are averages of 4 sweeps. Grey box indicates the timing of stimulus presentation.

F) Excitatory and inhibitory charge transfers calculated from the recordings in **E** and normalized to the maximum charge transfers plotted as a function of the distance from the inner radius of the ring stimulation to the soma. Blue trace is the excitatory receptive field and red trace is the inhibitory receptive field. Top axes show ring inner radius distance normalized to the maximum dendritic radius. For this cell, the maximum dendritic radius was 130 µm.

G) Excitatory charge transfer calculated for 4 cells plotted as a function of the length of the inner radius of the stimulus from the soma. Axes are normalized to the maximum charge transfer response and maximum dendritic radius, respectively. Blue and red lines are binned averages of the responses from each cell for excitation and inhibition, respectively; error bars/shading are S.D.

Figure S2. Procedure for determining locations of putative postsynaptic sites using kinetics of uncaging evoked events. Related to Figure 3.

We used event detection combined with selection of uncaging-evoked EPSCs with locally-maximal amplitudes to determine the location of putative postsynaptic sites.

A) Same recordings as in **Figure 3B** showing dendritic locations of detected uncaging-evoked events (*) and events further determined to be the sites of putative postsynaptic sites (#). For event detection, uncaging-evoked events were included if the amplitude was greater than 6 times the S.D of the baseline noise, measured during the 3 ms prior to uncaging. This conservative threshold was necessary because of the large amount of spontaneous activity in SACs. To determine putative postsynaptic sites, we identified locations along the dendrite in which the amplitude of uncaging-evoked currents were maximal relative to its neighbors within 5 μm (local maximum). This strategy minimized double counting, but could also lead to undercounting of putative postsynaptic sites for dendritic segments with high synapse density.

B) Dendritic locations of uncaging-evoked events. Each row is a different dendrite (n = 20 dendrites from 15 cells). The top row shows the event locations color-coded to match the traces in **A**.

C) Probability histogram of detecting events from **B** in 5 μm bins as a function of the path length from the soma.

D) Amplitude and rise time of uncaging-evoked events from the cell in **A** as a function of path length from the soma to the uncaging site. Putative postsynaptic sites were selected from uncaging-evoked events based on the amplitude of the events. Putative postsynaptic sites were defined as locally maximal in amplitude (filled circles) and the other events (open circles) were discarded. For well space-clamped locations proximal to the soma, the location of locally maximal amplitude almost always had locally minimal rise times, confirming the presence of a postsynaptic site. For distal locations, we did not observe the amplitude-rise time correlation, presumably due to dendritic filtering.

E) The path length for dendrites in **Figure 3C** from the most distal detected putative postsynaptic site ("last site") to the end of the dendrite plotted as a function of the total path length of the dendrite. The black line is a linear fit with $r^2 = 0.48$.

F) Rise time and amplitude of the uncaging-evoked events from putative postsynaptic sites from **Figure 3C-D** plotted as a function of path length from the soma.

G) The distance between pairs of adjacent putative postsynaptic sites from **Figure 3C-D** plotted as a function of the path length from the soma to the halfway point between each pair of putative postsynaptic sites.

To determine the minimum time between uncaging pulses to avoid uncaging when receptors were desensitized, we performed a paired-pulse experiment. We uncaged at the exact same location over a putative postsynaptic site and varied the interval between pulses to measure the desensitization period of the receptors.

H) Voltage clamp recordings (holding potential = -72 mV) from a SAC in response to glutamate uncaging at a single dendritic site. The time between pairs of uncaging pulses was varied and is listed to the left of each trace. Traces are averages of 10 sweeps.

I) Pair pulse ratio (PPR) as a function of the time between pulses for 5 dendritic sites from 3 cells. Grey lines = individual sites; solid grey line = the cell in **H**; black spots = the mean PPR across sites; error bars = S.D.

For 5 cells, we found a pair-pulse ratio equal to or greater than 1 when the time between uncaging pulses was 100 ms or more. Thus, we used intervals of 100 or 200 ms to map the uncaging responses.

Figure S3. Glutamate uncaging duration and resolution are sufficient to detect postsynaptic sites in distal dendrites if postsynaptic sites are present. Related to Figure 3.

We wanted to determine whether an absence of uncaging-evoked events in distal sites was due to an absence of receptors or the inability to record these currents from the soma. To test this, we performed two experiments. First, we increased the uncaging laser pulse duration while uncaging over distal dendrites to reveal the presence of AMPARs with a larger dose of glutamate.

A) SAC current responses (holding potential = -72 mV) to glutamate uncaging at 10 different dendritic sites (path length from soma indicated above traces) with three different laser pulse durations. The start of laser pulse illumination is indicated by the grey dashed lines. For part **A-C**, all traces are averages of 10 sweeps.

B) **i**: Expanded timescale of currents evoked at two adjacent dendritic sites from **A**.

ii: normalized uncaging-evoked currents at 101 um show a fast-rising response is detected at all laser pulse durations.

iii: Responses to 500 µs uncaging pulse at the two adjacent sites from **i** overlaid to demonstrate that sites not showing a response at short laser pulse durations never evoke fast-rising events, as would be expected if a prominent number of AMPARs were present at the site of uncaging. Note that because of the close location of the two sites, dendritic filtering also cannot account for the difference (see below for more detail).

C) Voltage clamp recordings (holding potential = -72 mV) from three cells in response to glutamate uncaging at very distal dendritic sites (path length from soma indicated to the left of the trace) using a 100 µs uncaging laser pulse demonstrating detection of glutamate receptors. Black traces were events detected using event detection criteria (see Methods), while adjacent grey traces were concluded to have no event.

We found that, while new events emerged when the pulse duration increased (**A**), these events display the typical kinetics of glutamate spillover (DiGregorio et al., 2007) (**B**, events recorded at >105 µm from soma), while synaptic sites showed a fast and slow phase typical of on-synapse activation followed by glutamate spillover onto the same synapse (events at <105 µm from the soma). Based on this experiment, we determined that the 100 µs uncaging laser pulse duration was sufficient for detection of distal synapses (**C**) while optimizing resolution and avoiding spillover.

Second, we examined theoretically whether there could be a decreased chance of detecting distal AMPAR clusters due to dendritic filtering.

D) and **E**) Numerical simulations of somatic EPSCs in a passive neuron under voltage-clamp (with C_m =1 pF/cm^2, R_m = 21700 Ω-cm^2, R_a = 100 Ω-cm or 200 Ω-cm. The amplitude of g_{syn} was set to reproduce experimental miniature EPSCs recorded from SACs (data not shown). Passive properties were assumed uniform across the cell. Pipette resistance was set at 20 MΩ. The idealized SAC dendritic morphology has a uniform diameter of 0.2 -0.4 µm (green, blue, and red traces), 3 dendritic branch points, and a maximum length of 150 µm.

D) Traces of simulated EPSCs in response to an evoked conductance (g_{syn}) at input locations at different path distances from the soma.

E) The peak amplitude of somatic EPSCs in response to a simulated evoked conductance at different path distances from the soma.

This simulation revealed that dendritic filtering, while present at distal sites, does not increase dramatically across the region of dendrite where the most distal synapses were observed, even for diameters as narrow as 0.2 µm. Thus we predict that currents arising from distal synapses should be detectable.

To determine whether the uncaging resolution is affected by the dendritic location of the uncaging site, we uncaged along lines perpendicular to sites previously determined to contain putative postsynaptic sites at different distances from the SAC soma. We determined the effective uncaging resolution by fitting the maximal responses to a Gaussian distribution and measuring the full-width half maximum (FWHM).

F) 2-photon fluorescence z-projection of a SAC showing locations of uncaging sites used to determine uncaging resolution (orange and pink lines). White asterisk = location of cell soma.

G) Amplitude of uncaging-evoked current as a function of the distance from the putative postsynaptic site to the uncaging site for the cell in **F**. Colored traces are voltage clamp recordings (holding potential = -72 mV) showing events detected by uncaging (averages of 10 sweeps). Solid black line is the Gaussian fit; the dotted line is the full-width half-max (FWHM) of the fit in microns.

H) The uncaging resolution (FWHM of the Gaussian fits determined as in **G**) as a function of the path length from the soma. The mean uncaging resolution was 2±0.6 µm (n=20 measurements from 11 dendrites in 8 cells). Grey dotted lines connect measurements from different sites on the same dendrite. Green line is a linear fit (slope = 0.002, r^2=0.013).

I) Rise time and amplitude of uncaging evoked events from dendritic locations in **H** plotted as a function of path length from the soma (n=20 measurements from 11 dendrites in 8 cells). Events shown were found to be closest to the peak amplitude of the Gaussian fits used to determine the uncaging resolution; colors correspond to the traces in that figure. Dotted lines connect samples measured from the same dendrite.

Figure S4. Effect of threshold on puncta detected from eight SACs labeled with PSD95-YFP. Related to Figure 4.
To identify PSD95 puncta, we computed the log ratio of the intensity of YFP fluorescence to tdTomato fluorescence for each pixel, $R=\log(F_{YFP}/F_{tdTomato})$. Variations in R are independent of imaging conditions that linearly scale the ratio of F_{YFP} and $F_{tdTomato}$ and help to normalize for bleed-through from the tdTomato channel into the YFP channel, which is more substantial in distal dendrites (see example images in **Figure 4C**). PSD95 puncta were subsequently identified using a segmentation algorithm that detected spatial variations of R. We systematically varied the threshold value of R to determine the effect of this value on the distribution of puncta as a function of distance along the dendrite. Across all cells, a threshold of R=1 represented a transition—a range of higher thresholds did not vary the distributions substantially while lower thresholds greatly increased the number of distal puncta. In addition, values of $R<1$ corresponded to F_{YFP} that was indistinguishable from $F_{tdTomato}$ bleedthrough (see example in **Figure 4A,C**).

A) First column: Skeleton analyzed dendritic arbors of all 8 cells with identified PSD95 puncta used for analysis (colored dots). Colors represent $R = \log(F_{YFP}/F_{tdTomato})$ within each punctum, which was used for thresholding puncta to include in subsequent analysis.
Second column: For each cell, the R value within each punctum (dots) is plotted as a function of path distance from the soma.
Third column: For each cell, the average linear density of PSD95 puncta as a function of path length from the soma is plotted using increasing thresholds of R to determine puncta to include in analysis.
All colors correspond to the colormap on the right.
B) This plot is the same as the plot in **Figure 4D** with the addition of three density lines showing additional threshold log ratios (green = 1.5; indigo = 0.5; black = 0.0), which demonstrate the average linear density of PSD95 puncta as a function of path length from the soma in 8 cells.
C) Histogram of PSD95 puncta (left axis) from 8 cells using a threshold log ratio of 1.0 (top; same as **Fig. 4E displayed for comparison**), 0.5 (middle), or 0.0 (bottom), as well as the synaptic contacts with DSGCs (right axis, black), as a function of radial distance from the soma. Radial distances of synaptic contacts with DSGCs were measured from electron microscopy reconstructions of 24 SACs (Briggman et al., 2011).

Figure S5. Synaptic input distribution supports direction selectivity of simulated dendritic voltage (PSD95 gradient). Related to Figure 5.

A) Ball-and-stick model of a partial SAC dendritic tree used for numerical simulations of dendritic integration. Blue circles indicate the location of synapses based on the distribution determined with PSD95 labeling (**Fig. 4**). Green arrows indicate locations where the dendritic voltage is measured.
B) Dendritic voltage at two of the locations indicated by the green arrows in **A**, in response to the outward (black traces) or inward (red traces) activation of the synapses displayed in **A** at a speed of 500 μm/s. Dotted lines indicate the amplitude of the peak of the synaptic response in each condition.
C) Heat map of dendritic voltage measured along the entire dendritic branch (x-axis) for the duration of the stimulus (y-axis) during which synapses, placed according to the average location of putative synapses determined from PSD95 labeling, are activated. The color scale depicts the amplitude of the depolarization. The left plot represents the response to outward stimulation, and the right plot the response to inward stimulation. At the peak of the activation of each synapse, the local voltage propagates with little electrotonic attenuation to the dendritic tip due to the end effect of the electrical cable. The green arrows above the plot indicate the two positions along the dendrite corresponding to the traces in **B** (25 and 95 μm from the soma), and the black arrows indicate the other locations where peak dendritic voltage is plotted on the summary plot (**Fig. 5I-J**).
D) Same as **A**, but blue circles indicate the location of regularly distributed synapses with the same average density as in A, the most distal synapse being located at the tip of the dendrite.
E) Same as **B**, but for the regular distribution of synapses extending to the tip of the dendrite, as displayed in **D**.
F) Same as **C**, but for the regular distribution of synapses extending to the tip of the dendrite, as displayed in **D**.
G) Somatic current clamp recordings from SACs during stimulation with moving squares presented over 75% (left) or 100% (right) of the dendritic radius. Responses to motion outward from the soma to the distal dendrites (black) and inward from the distal dendrites to the soma (red) are shown.
H) DS of the peak somatic voltage measured in current clamp during visual stimulation with moving squares traversing 75% or 100% of the dendritic radius. Data are from 9 cells in control conditions and 10 cells in the presence of 5 μm gabazine. Note the similarity between these recordings and the simulations of the voltage at 25 μm from the soma in **B**. Also note that the results shown in **G** and **H** here suggest that the SAC is not a passive cell, but rather has active conductances that alter the direction preference recorded at the soma.

Figure S6. Locations of visual stimulation and imaged varicosities. Related to Figure 6.

Maximum intensity z-projections of 2-photon images of SACs filled with OGB-1 with the laser tuned to 800 nm. Images were acquired after measuring Ca^{2+} transients in the varicosities indicated (magenta circles) in response to visual stimulation (see **Fig. 6**). Squares of light (25 μm) were projected on the retina along either 75 or 100% (**Fig. 7)** of the path indicated in green. The exact extent of stimulation relative to the SAC arbor was determined post-hoc from these images and corrected if necessary (e.g. SAC #8 below). Images are divided into two groups: SACs for which the imaged varicosity was located outside of the SAC's predicted excitatory receptive field (**top**) and SACs for which the imaged varicosity was within the SAC's predicted excitatory receptive field (**bottom**). Images within groups are ordered from left to right by the DSI of the indicated varicosity, starting with the varicosity with the strongest preference for outward motion at the top left.

The DS of varicosities was variable, as observed in previous studies (Euler et al., 2002; Hausselt et al., 2007; Lee and Zhou, 2006; Yonehara et al., 2013) (**Fig 6.**), which may arise from the following factors: 1) inability to optimally stimulate along the SAC dendritic path due to sometimes tortuous dendritic morphology (see SAC #18 below) and 2) limiting the stimulation to inward vs. outward may sub-optimally activate a varicosity whose preferred direction is slightly off this axis, as seen in other studies (Euler et al., 2002; Yonehara et al., 2013).

Figure S7. **Schematic of dendrite-autonomous contribution to circuit-level computation of motion direction. Related to Figure 7.**

A) i) Partial skeleton of a SAC showing the locations of the excitatory input region predicted from uncaging (blue), the varicosity-rich GABAergic output region (dark brown) and the overlapping region containing inputs and outputs (purple). The grey dotted lines show 75% and 100% of the dendritic radius. The details of this skeleton are based on reconstructions of starburst cells and therefore accurately reflect the dendritic features.
ii) The dendrite in **i** overlaid with a neighboring SAC dendrite (the same dendrite rotated 180°), with somas offset by 150 μm. The output regions of the two SACs overlap and provide opportunities for lateral inhibition between neighboring SACs.
iii) The grey dotted lines are in the same positions as in **i** and **ii**, demonstrating the regions of the neighboring SAC stimulated when the SAC in **i** is stimulated over 75% vs. 100% of its dendritic radius. A much larger region of the neighboring SAC is stimulated during 100% stimulation, which could produce an increase in lateral inhibition for the recorded cell, particularly during inward stimulation (inward relative to the recorded cell).

B) Schematic describing the enhancement of direction selectivity in SAC dendrites through SAC-SAC inhibitory interactions. Green cell indicates SAC filled with OGB via patch pipette (the recorded cell). White cell is a neighboring SAC. Excitatory bipolar cell inputs to SACs are blue circles, presynaptic GABA release sites on SACs are grey squares, and extent and direction of GABA release is indicated by size of red cloud and direction of red arrow, respectively. Extent of GABA release is assumed to correlate with the amplitudes of Ca^{2+} transients in putative release sites.
i) SAC-SAC interactions minimally affect SAC intrinsic direction selectivity during 75% stimulation.
Left: Outward stimulation of the recorded SAC produces a large calcium transient in its varicosities resulting in GABA release onto neighboring SACs. In contrast, the neighboring SAC experiences little excitation from this "inward" stimulation, which minimally enters its excitatory receptive field and does not induce strong summation of excitatory potentials at its varicosities. Therefore, no GABA is released onto the recorded SAC from the neighboring SAC and therefore there is minimal lateral inhibition.
Right: Inward stimulation of the recorded SAC reduces summation of excitatory potentials in its varicosities, resulting in a smaller calcium transient compared to outward stimulation. In addition, despite the stimulation minimally entering the excitatory receptive field of the neighboring SAC**,** the neighboring SAC experiences greater summation of excitatory potentials due to the "outward" stimulation it receives, resulting in a small release of GABA onto the recorded SAC. The small GABA release suppresses the calcium response in the varicosities of the recorded SAC, increasing its direction selectivity.
ii) SAC-SAC interactions enhance intrinsic SAC direction selectivity during 100% stimulation.
Left: Outward stimulation of the recorded SAC produces a large calcium transient in its varicosities, resulting in GABA release onto neighboring SACs. In contrast, outward stimulation also enters a large portion of the neighboring SAC's excitatory receptive field**,** but the "inward" stimulation does not induce strong summation of excitatory potentials at its varicosities and inhibition from antiparallel SACs further suppresses the response. Therefore, even though the 100% stimulus causes increased excitation onto the neighboring SAC compared to the 75% stimulus, the varicosities of the neighboring SAC still do not have enough Ca^{2+} influx to cause significant release of GABA onto the recorded SAC.
Right: Inward stimulation of the recorded SAC reduces summation of excitatory potentials in its varicosities, resulting in a smaller Ca2+ transient compared to outward stimulation. In addition, the stimulation activates a larger portion of the neighboring SACs excitatory receptive field than during the 75% stimulation. This increased outward stimulation of the neighboring SAC results in a large release of GABA onto the recorded SAC. The large GABA release further reduces the Ca^{2+} response in the varicosities of the recorded SAC, enhancing its direction selectivity about two-fold **(Figure 7)**.

In summary, SAC-SAC interactions serve to enhance the dendrite autonomous preference for outward motion we observe in SAC varicosities **(Figure 6)**. Importantly, dendrite autonomous direction selectivity also increases the importance of circuit level interactions; without the dendrite autonomous component of SAC direction selectivity, SAC-SAC signaling would cause GABA release onto a SAC even during outward motion, resulting in an overall reduction in SAC Ca^{2+} entry and a reduced preference for outward motion.

Supplemental Experimental Procedures

Visual stimulation and calcium imaging

Ethics statement
All animal procedures were approved by the UC Berkeley Institutional Animal Care and Use Committee and conformed to the NIH Guide for the Care and Use of Laboratory Animals, the Public Health Service Policy, and the SFN Policy on the Use of Animals in Neuroscience Research.

Tissue preparation
Adult mice (P21-P40) of either sex were anesthetized with isoflurane and decapitated. Retinas were dissected from enucleated eyes under infrared illumination and isolated retinas were mounted over a 1-2 mm^2 hole in filter paper (Millipore) with the photoreceptor layer side down. Mounted retinas were stored in oxygenated Ames' media (US Biological or Sigma) in the dark at room temperature prior to imaging and recording. To target SACs for whole cell recordings, we used two mouse lines that express fluorescent proteins in SACs: *mGluR2-GFP* mice that contain a transgene insertion of the interleukin-2 receptor fused to GFP under control of the mGluR2 promoter (Watanabe et al., 1998); and *ChAT-Cre/nGFP* mice generated by crossing a mouse in which IRES-Cre recombinase was knocked in downstream of the endogenous choline acetyltransferase gene (Ivanova et al., 2010) (B6.129S6-ChAT$^{tm2(cre)Lowl}$/J; Jackson Labs) (Chat-cre) with a mouse line containing a loxP-flanked STOP cassette upstream of the GFP gene containing a nuclear-localization sequence (Stoller et al., 2008) (B6.129-*Gt(ROSA)26Sor*^{tm1Joe}/J; Jackson Labs). For some experiments, ChAT-Cre mice without the nGFP transgene or wild-type (C57BL/6J; Jackson Labs) mice were used. In these experiments SAC identity was confirmed by fluorescence imaging of dye-filled cells at the end of the experiment.

Whole cell recordings
All recordings in this study were performed from displaced (On-layer) SACs. Retinas mounted on filter paper were placed under the microscope and perfused with oxygenated (95% O_2 – 5% CO_2), bicarbonate-buffered Ames' media at 32-34°C. For calcium imaging experiments, L-ascorbic acid (Sigma) was added to Ames' media to achieve a final concentration of 0.5 mM. For experiments in **Figure 7**, SR 95531 hydrobromide (GABAzine, Tocris Bioscience), was added to Ames' media to achieve a final concentration of 5 μM. Retinas were bathed in GABAzine-containing Ames' media for ≥ 10 minutes before recording from SACs.

To avoid bleaching the photoreceptors, fluorescently labeled retinal cells were targeted for whole cell recordings using two-photon microscopy (see *2-photon imaging* below) (Wei et al., 2010). For placing the patch pipette on the cell soma, the tissue was visualized using transmitted infrared illumination with an IR-LED (Thor Labs) and an IR1000 camera (DAGE-MTI). The inner limiting membrane and Müller cell endfeet above the targeted fluorescent cell were removed using a glass pipette before targeting a new pipette for recording. In all instances a gigaohm seal was obtained before breaking in.

For whole cell voltage clamp recordings, borosilicate glass electrodes pulled to a 5-7MΩ tip were filled with an internal solution containing (in mM): 110 CsMeSO3, 2.8 NaCl, 4 EGTA, 5 TEA-Cl, 4 adenosine 5'-triphosphate (magnesium salt), 0.3 guanosine 5'-triphosphate (trisodium salt), 20 HEPES, 10 phosphocreatine (disodium salt), and CsOH to pH 7.2. Alexa Fluor 594 hydrazide (0.03 mM, Life Technologies, #A-10438) was included in internal solution for collecting 2-photon images of dendritic morphology after the visual stimulation protocol was complete. Voltage clamp recordings were acquired at 10 kHz and filtered at 2 kHz with a Multiclamp 700A amplifier (Molecular Devices) using pCLAMP 10 recording software and a Digidata 1440 digitizer. Currents were recorded at only one holding potential (-72 mV). The holding potentials reported throughout are after correction for the junction potential (-12 mV).

For calcium imaging experiments, electrodes were filled with an internal solution containing (in mM): 116 D-gluconic acid (K+ salt), 6 KCl, 2 NaCl, 20 HEPES, 4 adenosine 5'-triphosphate (magnesium salt), 0.3 guanosine 5'-triphosphate (trisodium salt), 10 phosphocreatine (disodium salt), 0.15 Oregon Green 488 BAPTA-1 hexapostassium salt (OGB-1; Life Technologies) and KOH to pH 7.25. Membrane potentials reported here are after correction for the liquid junction potential (-8.6mV) Cells were held in current clamp for calcium imaging experiments and recordings were acquired at 10kHz. Cells resting above -48 mV were injected with negative current (maximum -150 pA) to achieve a resting potential < -48mV. Cells that did not hyperpolarize below -48mV upon current injection were discarded from analysis.

2-photon imaging

Targeted patching of GFP-expressing cells and imaging of Alexa-594 and OGB-1 dye-filled SACs were performed using a custom-built two-photon microscope. We used a Chameleon Ultra II laser (Coherent) tuned to 810 nm (for Alexa-594 dye imaging) or 930 nm (for GFP and OGB-1 imaging) focused through a 60x LUMPlanFL N water-immersion objective (1.00 NA, Olympus). A 20x UMPlanFL N water-immersion objective (0.50 NA, Olympus) was used for imaging the entire SAC dendritic tree. Laser intensity was controlled using a Pockels cell (Conoptics), scanning was performed using a 3 mm XY Galvanometer scanner (Edmund Optics), and the fluorescence was collected with photomultiplier tubes (H10770PA-40, Hamamatsu). The average sample plane laser power measured after the objective was 6.5-13 mW. The imaging system was controlled by ScanImage software (www.scanimage.org).

For Ca^{2+} imaging experiments, OGB-1 visualization was performed at 930 nm to reduce the light response of the retina during scanning (Denk and Detwiler, 1999). After break-in, the distal end of a dendrite, as well as a single varicosity on that dendrite, were identified as quickly as possible with minimal exposure to the 2-photon laser (6±2 minutes after break in). A small region of interest (2-6 μm^2) that included the varicosity was imaged at either 5.92 or 11.84 Hz (64 x 64 pixels) (see *Visual Stimulation* below). Unlike Hausselt et al. (2007), we saw that a majority (61%) of our patched SACs had Ca^{2+} responses to light stimuli, although long whole cell recording times (>~20 minutes), as well as prolonged laser and/or visual stimulation exposure, often led to unreliable Ca^{2+} responses. These included changes in SAC response polarity (Vlasits et al., 2014), as assessed by the electrical current clamp recording, as well as reduction in fluorescent signal and light responsiveness. Cells were discarded from analysis if the response polarity changed during the imaging session or if the responses to stimuli were lower than 2 S.D. above the noise. Overall, 39% of cells for which a recording was achieved were discarded for the reasons stated above.

Visual Stimulation

For visual receptive field mapping using voltage clamp, visual stimuli were generated using a computer running an Intel core duo processor with Windows XP running a monochromatic organic light-emitting display (OLED-XL, eMagin, 800 x 600 pixel resolution, 85 Hz refresh rate). For simultaneous calcium imaging and visual stimulation, visual stimuli were generated using a computer running an Intel core duo processor with Ubuntu (v. 14.04.2, "Trusty Tahr") running a DMD projector (Cel5500-Fiber, Digital Light Innovations, 1024 x 768 pixel resolution, 60 Hz refresh rate) and an LED light source (M470L2, Thorlabs, Inc.). Visual stimuli were filtered to project only wavelengths between 480-490 nm. The OLED or DMD was projected through a condenser lens onto the photoreceptor-side of the sample. For the OLED, the maximum size of the projected image on the retina was 800 x 600 µm. For the DMD, the maximum size of the projected image on the retina was 670 µm x 500 µm. Custom stimuli were developed using Matlab or GNU Octave and the Psychophysics Toolbox. Proper alignment of stimuli in all planes was checked each day prior to performing the experiment. First, a pipette filled with fluorescent dye was inserted into the bath at the focal plane of the retinal photoreceptors in our chamber (empirically measured using IR imaging (see *Whole Cell Recordings*)). The tip of the pipette was used to find the center of the 2-photon image and align it to a point in the image from the IR1000 camera used for patching. A 5 µm radius spot was then projected through the condenser and detected directly with the IR1000 camera. To align the stimulus to the tip of the pipette (center point of the 2-photon image) any misalignments in the z-plane were corrected by focusing the condenser, while those in the x-y plane were corrected by shifting the condenser along the horizontal axes.

For visual receptive field mapping with voltage clamp, we presented 4 repetitions of each stationary spot (12.5 µm radius) position at maximum intensity (2.9 x 10^5 R*/rod/s) on a black background (1.4 x 10^4 R*/rod/s) for 1 s with 2 s between each spot. For rings, we presented 4 repetitions of each ring radius at maximum intensity (2.9 x 10^5 R*/rod/s) on a dark grey background (8.3 x 10^4 R*/rod/s) for 1 s with 2 s between each ring. For rings and spots, we allowed the retina to adapt to the background illumination for 30 s before beginning data collection. After the experiment was performed a 1 µm/slice z-stack of the dye-filled dendritic arbor was acquired to determine stimuli locations.

For simultaneous calcium imaging and visual stimulation, we first calculated the dendritic radius of a SAC using measurement tools in ImageJ on images of the dye-filled arbor and soma taken within 15 minutes of break-in (See *Data Analysis* for radius calculations). For **Fig. 2**, we presented 3 repetitions of the same sized stationary spot (12.5µm radius) (1.9 x 10^5 R*/rod/s) on a black background for 1 s with 6 s between each spot. Spots were centered on the 25-100% dendritic radius locations previously calculated from ImageJ. For measuring direction selectivity (**Fig. 6**), we presented a 25 µm x 25µm square moving at 500 µm/s. For outward moving squares, the stimulus originated centered on the soma and moved a distance of 75 or 100% of the dendritic radius. Inward stimuli began centered at either 75% or 100% of the dendritic radius and moved inward to the soma. For both these experiments, the relative visual stimulus location along the SAC arbor was verified, and post-hoc corrected if necessary, using a

maximum intensity projection image of a .5 um/slice z-stack of the quadrant of the filled SAC containing the region of interest imaged. The stack was acquired with the laser tuned to 800 nm (16 mW sample plane power) to take advantage of the larger 2-photon cross-section of OGB at this wavelength. For all visual stimulation experiments, stimuli were presented in pseudorandom order.

Data analysis

Data analysis of physiological recordings was performed in IgorPro (WaveMetrics) running Neuromatic functions. Reported responses are the averages over the 4 repetitions of each stimulus position/radius. The excitatory charge transfer of visually-evoked events was calculated by integrating the average current over the entire 1 s period of the stimulus and subtracting the background charge measured during the 1 s prior to stimulus presentation. For spots, the charge transfer was normalized to the charge transfer measured at the soma as this was usually the maximum response (**Fig. 1B-E**). For rings, the charge transfer was normalized to the maximum charge transfer (**Fig. 1F-I**). For spots, the receptive field was defined as the % of the dendritic field at which the normalized charge transfer reached <5% of the charge transfer at the soma. For rings, the receptive field was defined as the % of the dendritic field at which the normalized charge transfer reached <0% of the maximum charge transfer.

Measurements of the extent of the SAC dendritic field were performed in ImageJ. Measurements were taken from the maximum intensity projection of images of the SAC. The dendritic field with stationary spot stimuli (**Fig. 1B-E**) was the radius from the center of the soma to the edge of the longest dendrite within the region of the cell covered by the stimuli. The dendritic field with ring stimuli (**Fig. 1F-I**), was the radius from the center of the soma to the end of the longest dendrite in the entire dendritic tree. The dendritic field for Ca^{2+} imaging experiments was the radius from the center of the soma through the imaged varicosity to the edge of the longest dendrite within the region of the cell covered by the stimuli. Path lengths were calculated using the segmented line function in ImageJ to trace the dendritic path from the soma through the imaged varicosity to the tip of that dendrite.

Analysis of the calcium imaging experiments was performed in MATLAB and IgorPro using custom procedures. Images of varicosities were segmented by Multi Otsu's method. In brief, time-lapse images from a single stimulation experiment were combined by maximum intensity projection. The bottom class of each thresholded projection was then assigned as background, while the top class was used as a mask for further analysis. The pixel intensities for pixels within a mask were averaged at each time step. The average background intensity was subtracted and the change in fluorescence responses shown here were calculated as

$$\frac{\Delta F}{F} = \frac{F - F_0}{F_0}$$

where F is the fluorescence during visual stimulation and F_0 is the average fluorescence during the 3 s preceding visual stimulation. The maximum ΔF/F for each average response was used to calculate the direction selectivity index as follows (with direction of visual stimulation relative to SAC soma indicated by the subscript):

$$\frac{\frac{\Delta F}{F}_{out} - \frac{\Delta F}{F}_{in}}{\frac{\Delta F}{F}_{out} + \frac{\Delta F}{F}_{in}}$$

Glutamate Uncaging

Ethics statement

Animal experiments were performed in accordance with the guidelines of Institut Pasteur.

Tissue preparation

Tissue was prepared as described for visual stimulation (above) with the exception that dissections of the retina were done in ambient light and tissue was stored in oxygenated ACSF containing (in mM): 125 NaCl, 2.5 KCl, 1 $CaCl_2$, 1 $MgCl_2$, 1.25 NaH_2PO_4, 25 $NaHCO_3$, and 25 glucose. We recorded from wild type (C57Bl/6) mice. To target On-SACs in wild type mice, we filled cells with small, round somas (Petit-Jacques et al., 2005) with Alexa Fluor 594 in the internal solution and imaged the dendritic morphology using a 2-photon microscope to determine cell identity before proceeding.

Voltage clamp recordings

Whole-cell recordings were made from SACs at -72 mV at near physiological temperatures (32°C) using a Multiclamp 700B amplifier (Axon Instruments, Foster City, Ca, USA) with thick-walled glass patch-electrodes (tip resistances of 5-8 MΩ) that were backfilled with either a K^+-based internal solution containing (in mM): 117 K-$MeSO_3$, 40 HEPES, 6 NaOH, 5 EGTA, 1.78 $CaCl_2$, 4 MgCl2, 0.3 NaGTP, 4 NaATP, and 0.03 Alexa 594 or a Cs^+-based internal solution containing (in mM): 90 Cs-$MeSO_3$, 40 HEPES, 6 NaOH, 10 BAPTA, 3.4 $CaCl_2$, 5 $MgCl_2$, 10 TEA-Cl, 0.3 NaGTP, 4 NaATP, and 0.03 Alexa 594, adjusted to ~305 mOsm and pH 7.3. The series resistance was typically below 35 MΩ and was not compensated. Unless otherwise noted, for recording, the ACSF was supplemented with 2 μM L-AP4 and 1.2 μM LY341495 to block the light response from photoreceptors (Ala-Laurila et al., 2011) in addition to 2 mM MNI-glutamate. Uncaging-evoked events were filtered at 10 kHz and digitized at 100-500 kHz using an analogue-to-digital converter (model NI USB 6259, National Instruments, Austin, TX, USA) and acquired with Nclamp (www.neuromatic.thinkrandom.com).

2-photon imaging

SAC somata were identified and whole-cell patched using infrared Dodt contrast (Luigs and Neumann, Ratingen, Germany) and a frame transfer CCD camera (Scion Corporation, Cairn Research Ltd, Faversham, UK). These components were mounted on an Ultima two-photon laser scanning head (Prairie Technologies, Middleton, WI, USA) based on an Olympus BX61W1 microscope, equipped with a water- immersion objective (60x, 1.1 numerical aperture, Olympus Optical, Tokyo, Japan). Two-photon excitation was performed with a pulsed Ti:Sapphire laser (DeepSee, Spectra-Physics, Evry, France) tuned to 810 nm. The SAC morphology was visualized from maximal intensity projections of 2PLSM images (0.261 μm/pixel, and 1 μm in Z-dimension) to find isolated dendrites for uncaging. 100 nm diameter fluorescent beads (Invitrogen, Carlsbad, CA, USA) were used to estimate the point spread function (PSF) of the microscope system as previously described (Abrahamsson et al., 2012; DiGregorio et al., 2007). The measured PSF had lateral and axial dimensions of 390 ± 5 nm (FWHM, n = 15) and 1430 ± 40 nm (n = 14), respectively.

Glutamate uncaging

The caged compound 4-methoxy-7-nitroindolinyl-caged L-glutamate (MNI-glutamate, Tocris Bioscience) was bath applied at a concentration of 2 mM (in ACSF). The custom photolysis system was coupled into the photolysis pathway of the Ultima two-photon scanhead. A 405 nm diode laser (Omicron Lasers, Rodgau, Germany) beam was coupled to the microscope using a single mode optical fiber (Oz Optics, Ottawa, Ontario, Canada) similar to a previously described setup (DiGregorio et al., 2007), except additional optics were used to adjust the convergence angle to both backfill the objective and match the focal plane of the two photon excitation for imaging (810 nm). Parfocality of the two wavelengths was verified previously (Abrahamsson et al., 2012). Photolysis laser powers were 2.55 mW.

To map putative postsynaptic sites along a dendrite (**Fig. 3**), we uncaged at dendritic locations 2.5-4 μm apart at 100 or 200 ms intervals and measured current responses to uncaging in voltage clamp. In one cell, we uncaged inward from the distal dendrite to the soma and did not observe any differences in measured parameters (data not shown). Uncaging-based mapping was performed using 100 μs duration laser pulses, a duration shown to optimize event detection and resolution (see **Fig. S2**). The effective uncaging resolution was measured by uncaging systematically in locations 0.5 – 1 μm along a line perpendicular to a synaptic location determined via mapping (**Fig. S3**). For all experiments, uncaging pulses in neighboring locations were timed 100 or 200 ms apart, which was enough time to ensure that nearby glutamate receptors were no longer desensitized (**Fig. S2**). Depending on flatness of the sample, the objective was refocused between bouts of uncaging to only uncage on in-focus sections of the dendrite. Because SAC dendrites lie in a relatively flat plane, tissue depth was fairly constant across uncaging locations, though because of slight changes in depth of the dendrites in the inner plexiform layer, we cannot make major conclusions about receptor number or dendritic filtering using amplitudes of events measured here.

Data analysis

Data analysis of uncaging-evoked events was performed in IgorPro (WaveMetrics) running Neuromatic functions. Using event detection combined with selection of events with locally-maximal amplitudes, we determined the events we thought were putative postsynaptic sites (**Fig. S2**).

For event detection, uncaging-evoked events were defined as having an amplitude greater than 6 times the S.D. measured during the 3 ms prior to uncaging. This criterion was found to be sufficient to exclude noise due to spontaneous activity from being included. The amplitude was defined as the maximum current during the 10 ms after uncaging. The rise time was the time period from 10% to 90% of the amplitude.

For analyzing the resolution of uncaging, we evaluated the event found to have the maximum amplitude to determine the time point for evaluating the amplitude of other events in the series. These amplitudes were then fit to a Gaussian distribution and the FWHM of the distribution was measured to determine the resolution of uncaging. The paired-pulse ratio was defined as the amplitude of the second uncaging event divided by the first event.

To determine the location of putative postsynaptic sites from uncaging-evoked events, we selected the events of local maximal amplitude within 5 μm from the set of events detected using the event detection procedure described above (**Fig. S2**). For events proximal to the soma, events with locally maximal amplitude almost always had locally minimal rise times, while for events distal to the soma this was not the case (**Fig. S2**).

The path length from the soma to the location of the uncaging sites was determined in ImageJ. Measurements were taken from the maximum intensity projection of images of the SAC (stacks taken in 1 μm z-steps). We traced the path from the center of the soma to most distal uncaging site recorded in an image during the experiment identified based on the local anatomical features. Then, we extrapolated backward from this site to the soma to determine the location of all other sites using our records of the distance between sites measured during the experiment. For analyses using the radius from the soma to distal uncaging sites, we measured the radius using a straight line from the soma center to the anatomical location of the most distal uncaging site. The dendritic field was measured from a straight line from soma center to the end of the dendrite uncaged upon. The receptive field was defined as the % of the dendritic field at which the last synaptic site was detected.

PSD95 Labeling and Imaging

Ethics statement

This study was conducted with the approval of the University of Washington Institutional Animal Care and Use Committee (Protocol 4122-01). Mice were euthanized by isoflurane overdose followed by decapitation.

Tissue preparation

Mice of postnatal day 22 were euthanized and enucleated and the eyes immersed in oxygenated mouse artificial cerebral spinal fluid (mACSF) containing the following in (mM): 119 NaCl, 2.5 KCl, 2.5 $CaCl_2$, 1.3 $MgCl_2$, 1 NaH_2PO_4, 11 glucose, and 20 HEPES, and brought to pH 7.42 with NaOH. To obtain retinal whole mounts, retinas were isolated in mACSF and mounted flat, ganglion cell side up, onto filter paper (Millipore).

Biolistic transfection

Plasmids for which a cytomegalovirus (CMV) promoter drives expression of tandem dimer Tomato (tdTomato) or postsynaptic density protein 95 fused to yellow fluorescent protein (PSD95YFP) were coprecipitated onto gold particles (Bio-Rad) (Morgan and Kerschensteiner, 2012). Gold particles were propelled into whole mount retinas using a Helios Gene Gun (Bio-Rad), and the tissue then incubated at ~34°C in oxygenated mACSF in a humidified chamber for 24 hr to allow for expression of PSD95 and tdTomato. We have found that 18-24 hour incubation is sufficient for detection of fluorescent protein expression in peripheral processes (Morgan et al., 2008), and minimizes overexpression of exogeneous PSD95 which is accompanied by accumulation of fluorescent protein in the nucleus, indicative of overexpression, and is known to alter synaptic dynamics (El-Husseini et al., 2000; Prange et al., 2004). Afterwards, retinas were fixed in 4% paraformaldehyde in mACSF for 20-30 min, rinsed in PBS, and flat mounted in vectashield (Vector Laboratories) for confocal imaging.

Image acquisition

Image stacks were acquired on an Olympus FV-1000 laser scanning confocal microscope with an oil-immersion 60x objective (Olympus, 1.35 NA). Voxel dimensions were (x-y-z in μm) 0.103-0.103-0.3 for images of isolated single starburst amacrine cells (SACs) in whole mount retinas. Images were median filtered to remove noise and compressed to 8-bits for analysis after normalization of the entire stack histogram using Fiji(Schindelin et al., 2012).

Quantification of SAC dendrites

The branching patterns of SAC dendrites were skeletonized using the filament function of Imaris (Bitplane). Total dendritic length was calculated from the skeletonized filament. A skeleton of an entire SAC traced in Imaris was used to create the schematic in **Figure S6**.

Identification and quantification of postsynaptic PSD95 puncta

Potential PSD95YFP puncta were identified using custom MATLAB scripts previously described(Morgan et al., 2008). Briefly, fluorescence signals within the PSD95 channel were iteratively thresholded, filtered by size and

contrast, and their ratio of fluorescence to cytosolic fluorescence intensity. We then calculated the log ratio of YFP to tdTomato fluorescence intensity within each punctum in order to evaluate potential bleedthrough between the two channel (Torborg and Feller, 2004). To compare across cells, for each cell, the minimum value for the log ratio for each cell was set to zero (but log ratio distributions were not normalized). A log ratio threshold of 1 was used for simulations and comparison to uncaging and output distributions because it minimized bleedthrough while allowing for a clear designation of PSD95 puncta (see **Fig. S4** for details). For figures in which a log ratio threshold is used, only puncta with a log ratio greater than the threshold value were included in analysis.

Path length and radial density analysis

We first determined the path length distance from the soma for every node of the skeletonized dendritic filament. The path length distance for each PSD95 puncta was assigned from its nearest node of the skeletonized dendritic filament. We determined the path length puncta linear density by dividing the total number of identified PSD95 puncta by the total dendritic length of the skeletonized dendrite within a sliding window of 10 µms, incrementally by 1 µm, from the soma to the longest path length distance. For radial distributions in **Figure 4E** and **Figure S4C**, the number of inputs across cells was summed in 1 µm bins. To exclude the cell body and vertical dendritic segments the initial 15 µm were omitted.

Simulation of SAC

Passive cable simulations of EPSC propagation or EPSP integration within an idealized SAC model were performed using Neuron v7.3 (Carnevale and Hines, 2006). The SAC morphology was approximated as a ball-and-stick model (**Fig. 5**, **Fig S3, and Fig. S5**).

To test the effect of dendritic filtering on voltage-clamp recordings, we modeled one 150 µm-long main dendritic branch, each with 3 branch points at 15, 35 and 65 µm **(Fig. S3)**. This length was chosen to correspond to the longest SAC dendrites measured (3% of 95 dendrites of SACs patch-loaded with Alexa Fluor 594 and imaged on a two-photon microscope), for which distal events would be the most filtered.

For the integration experiments, we wanted to establish an average dendritic branching representative of SAC morphology **(Fig. 5, Fig. S5)**. Out of the 95 dendrites of SACs imaged and measured, 66% had 4 of 5 orders of branching, so we implemented those two morphologies in the model. We modeled one 105 µm-long main dendritic branch, with 4 branch points at 10.9, 35.2 and 67.2 and 73.7 µm, and another 115 µm-long main dendritic branch, with 3 branch points at 21.9, 53.6 and 69.1 µm. Synapses were distributed along one of the main branches with regular spacing or as a density gradient that matched experimental findings. The initial 10 µm of the dendrite was set to 400 nm in diameter, which represents the dendritic segment linking the soma in the ganglion cell layer to the dendrites in the inner plexiform layer. The diameter of subsequent dendrites were set at a constant value of 200 nm (Kim et al., 2014). Varicosities were inserted in the most distal third of the dendrites, equally spaced, and modeled as a cylinder of 500 nm length and 500 nm diameter.

Passive properties were assumed uniform across the cell. Specific membrane capacitance (C_m) was set to 1 pF/cm². R_m was set to 21700 Ω-cm² based on an electrophysiological estimate of the membrane time constant (t_m = 21.7±2.4ms, n=5 cells, data not shown). t_m was measured from the slowest decay time constant of the voltage response to a brief 0.5 ms negative current pulse injection, which produced hyperpolarizations of 30 mV. R_i was set to either 100 Ω-cm or 200 Ω-cm to match a range of values used in modeling studies of SACs and other amacrine cells (Grimes et al., 2010; Singer et al., 2004; Tukker et al., 2004). In all simulations, the resting potential of the cell was set at -70 mV.

All synaptic responses were modeled using the Exp2syn function. The AMPA conductance was set to match the amplitude (313 pS) and time course (t_{rise} = 0.14ms, t_{decay} = 0.54ms) of fast rising miniatures EPSCs (< 0.175 ms rise-time, data not shown), as they are likely to represent synapses converging on proximal dendritic compartments, which are space-clamped. For direction selectivity simulations, however, the value of the synaptic conductance was increased to model the release of three vesicles (939 pS) to account for multivesicular release from bipolar cell terminals (Grimes et al., 2010). We plotted the simulated dendritic voltage at 25, 55, 75, 95 and 105 or 115 µm from the soma, in response to the inward or outward activation of synapses at a speed of 500 µm/s. This speed is within the range of velocity tuning of direction-selective ganglion cells (Sivyer et al., 2010) and matches the speed of visual stimulation from experiments in **Figures 6** and **7**.

Supplemental References

Abrahamsson, T., Cathala, L., Matsui, K., Shigemoto, R., and Digregorio, D.A. (2012). Thin dendrites of cerebellar interneurons confer sublinear synaptic integration and a gradient of short-term plasticity. Neuron *73*, 1159–1172.

Ala-Laurila, P., Greschner, M., Chichilnisky, E.J., and Rieke, F. (2011). Cone photoreceptor contributions to noise and correlations in the retinal output. Nat. Neurosci. *14*, 1309–1316.

Carnevale, N.T., and Hines, M.L. (2006). The NEURON book (Cambridge, UK: Cambridge University Press).

Denk, W., and Detwiler, P. (1999). Optical recording of light-evoked calcium signals in the funtionally intact retina. Proc. Natl. Acad. Sci. *96*, 7035–7040.

DiGregorio, D.A., Rothman, J.S., Nielsen, T.A., and Silver, R.A. (2007). Desensitization properties of AMPA receptors at the cerebellar mossy fiber granule cell synapse. J. Neurosci. *27*, 8344–8357.

El-Husseini, A., Schnell, E., Chetkovich, D., Nicoll, R.A., and Bredt, D.S. (2000). PSD-95 involvement in maturation of excitatory synapses. Science (80-.). *290*, 1364–1369.

Grimes, W.N., Zhang, J., Graydon, C.W., Kachar, B., and Diamond, J.S. (2010). Retinal parallel processors: more than 100 independent microcircuits operate within a single interneuron. Neuron *65*, 873–885.

Hausselt, S.E., Euler, T., Detwiler, P.B., and Denk, W. (2007). A dendrite-autonomous mechanism for direction selectivity in retinal starburst amacrine cells. PLoS Biol. *5*, e185.

Ivanova, E., Hwang, G.-S., and Pan, Z.-H. (2010). Characterization of transgenic mouse lines expressing Cre recombinase in the retina. Neuroscience *165*, 233–243.

Kim, J.S., Greene, M.J., Zlateski, A., Lee, K., Richardson, M., Turaga, S.C., Purcaro, M., Balkam, M., Robinson, A., Behabadi, B.F., et al. (2014). Space–time wiring specificity supports direction selectivity in the retina. Nature *509*, 331–336.

Morgan, J.L., and Kerschensteiner, D. (2012). Coating gold particles with DNA (biolistics). Cold Spring Harb. Protoc. *2012*, 114–117.

Morgan, J.L., Schubert, T., and Wong, R.O.L. (2008). Developmental patterning of glutamatergic synapses onto retinal ganglion cells. Neural Dev. *3*, 8.

Petit-Jacques, J., Völgyi, B., Rudy, B., and Bloomfield, S. (2005). Spontaneous oscillatory activity of starburst amacrine cells in the mouse retina. J. Neurophysiol. *94*, 1770–1780.

Prange, O., Wong, T.P., Gerrow, K., Wang, Y.T., and El-Husseini, A. (2004). A balance between excitatory and inhibitory synapses is controlled by PSD-95 and neuroligin. Proc. Natl. Acad. Sci. *101*, 13915–13920.

Schindelin, J., Arganda-Carreras, I., and Frise, E. (2012). Fiji: an open-source platform for biological-image analysis. Nat. Methods *9*, 676–682.

Singer, J.H., Lassová, L., Vardi, N., and Diamond, J.S. (2004). Coordinated multivesicular release at a mammalian ribbon synapse. Nat. Neurosci. *7*, 826–833.

Sivyer, B., van Wyk, M., Vaney, D.I., and Taylor, W.R. (2010). Synaptic inputs and timing underlying the velocity tuning of direction-selective ganglion cells in rabbit retina. J. Physiol. *588*, 3243–3253.

Stoller, J.Z., Degenhardt, K.R., Huang, L., Zhou, D.D., Lu, M.M., and Epstein, J. a (2008). Cre reporter mouse expressing a nuclear localized fusion of GFP and beta-galactosidase reveals new derivatives of Pax3-expressing precursors. Genesis *46*, 200–204.

Torborg, C.L., and Feller, M.B. (2004). Unbiased analysis of bulk axonal segregation patterns. J. Neurosci. Methods *135*, 17–26.

Tukker, J.J., Taylor, W.R., and Smith, R.G. (2004). Direction selectivity in a model of the starburst amacrine cell. Vis. Neurosci. *21*, 611–625.

Vlasits, A.L., Bos, R., Morrie, R.D., Fortuny, C., Flannery, J.G., Feller, M.B., and Rivlin-Etzion, M. (2014). Visual Stimulation Switches the Polarity of Excitatory Input to Starburst Amacrine Cells. Neuron *83*, 1172–1184.

Watanabe, D., Inokawa, H., and Hashimoto, K. (1998). Ablation of cerebellar Golgi cells disrupts synaptic integration involving GABA inhibition and NMDA receptor activation in motor coordination. Cell *95*, 17–27.

Wei, W., Elstrott, J., and Feller, M.B. (2010). Two-photon targeted recording of GFP-expressing neurons for light responses and live-cell imaging in the mouse retina. Nat. Protoc. *5*, 1347–1352.